19th AIAA Computational Fluid Dynamics
22 - 25 June 2009, San Antonio, Texas

AIAA 2009-3785

# A Spectral Difference method for viscous compressible flows with shocks

Sachin Premasuthan, * Chunlei Liang † and Antony Jameson ‡
*Stanford University, Stanford, CA 94305, USA*

**The current work focuses on applying an artificial viscosity approach to the Spectral Difference (SD) method to enable high-order computation of compressible fluid flows with discontinuities. The study uses an artificial viscosity approach similar to the high-wavenumber biased artificial viscosity approach introduced by Cook and Cabot,[5,6] and modified by Kawai and Lele.[9] The model employs a bulk viscosity for treating shocks, a shear viscosity for treating turbulence, and an artificial conductivity to handle contact discontinuities. The high-wavenumber biased viscosity is found to stabilize numerical calculations and reduce oscillations near discontinuities. Promising results are demonstrated for 1-D and 2-D test problems.**

## I. Introduction

Until recently, compressible flow computations on unstructured meshes have generally been dominated by schemes restricted to second order accuracy. However, the need for highly accurate methods in applications such as large eddy simulation, direct numerical simulation, computational aeroacoustics etc., has seen the development of higher order schemes for unstructured meshes such as the Discontinuous Galerkin (DG) Method,[2,13] Spectral Volume (SV) method[12,25] and Spectral Difference (SD) Method.[11,23] The SD method is a newly developed efficient high-order approach based on differential form of the governing equation. It was originally proposed by Liu et al.[11] and developed for wave equations in their paper on triangular grids. Wang et al.[23](2007) extended it to 2D Euler equations on triangular grids and Sun et al.[24](2007) further developed it for three-dimensional Navier-Stokes equations on hexahedral unstructured meshes. The SD method combines elements from finite-volume and finite-difference techniques, and is particularly attractive because it is conservative, has a simple formulation and straightforward implementation.

One of the greatest challenges with using high-order unstructured solvers is their inability to handle flow discontinuities. When flows involve steep gradients such as shock waves or contact surfaces, non-physical spurious oscillations arise that cause the simulations to go unstable. For higher order approximations, it is typically necessary to add explicit dissipation in order to obtain a stable solution. But this has a negative effect on accuracy, and the resolution of turbulent scales. The development of numerical algorithms that capture discontinuities and also resolve the scales of turbulence in compressible turbulent flows remains a significant challenge.

A classical approach to shock capturing is the addition of artificial viscosity, pioneered by von Neumann and Richtmeyer.[14] Cook and Cabot proposed such a method for high-order centered differencing schemes, wherein a spectral-like high-wavenumber biased artificial viscosity and diffusivity were dynamically added.[5,6] This was followed up with work by Fiorina and Lele,[7] on high-order compact difference schemes, wherein artificial diffusivity was added in addition to artificial viscosity. Kawai and Lele[9] extended the method to non-uniform and curvilinear meshes. This method involves the dynamic addition of grid-dependent localized transport coefficients such as artificial bulk viscosity, shear viscosity, artificial conductivity where needed. This facilitates the capturing of discontinuities by smearing the discontinuity over a numerically resolvable scale. The application of this form of artificial viscosity (hyperviscosity) has been limited to structured grid computations.

*Doctoral Candidate, Department of Aeronautics and Astronautics, Stanford University, AIAA Member.
†Post-Doc, Department of Aeronautics and Astronautics, Stanford University, AIAA Member.
‡Professor, Department of Aeronautics and Astronautics, Stanford University, AIAA Fellow.

Other forms of artificial viscosity have been applied to high-order unstructured grid calculations. Persson and Peraire[15] introduced a p-dependent artificial viscosity and demonstrated that higher-order representations and a piecewise-constant artificial viscosity can be combined to produce sub-cell shock resolution. Barter and Darmofal[3] proposed shock-capturing using a combination of higher-order PDE-based artificial viscosity and enthalpy-preserving dissipation operator. Both the above methods were proposed for high-order Discontinuous Galerkin (DG) discretizations.

The current study focuses on extending the artificial viscosity approach proposed by Cook et al,[5,6] and modified by Kawai et al[9] to computations on unstructured quadrilateral grids using the Spectral Difference scheme. This paper will discuss the salient aspects of implementing artificial viscosity within the Spectral Difference setup. A number of test-cases in 1D and 2D will be included to demonstrate its applicability as well as limitations. The current implementation of artificial viscosity can also be easily extended to 3D spectral difference scheme.

In section II, we look at the formulation of the Spectral Difference (SD) method on unstructured quadrilateral meshes. Section III discusses the details of the artificial viscosity method used. In section IV, we look at the numerical results obtained from the application of the artificial viscosity method to 1-D and 2-D test cases. Section V discusses the conclusions of our study and the direction of future efforts.

## II. Formulation of 2D Spectral Difference Scheme on quadrilateral meshes

The formulation of the equations for the 2D spectral difference scheme on quadrilateral meshes is similiar to the formulation of Sun et al[24] for unstructured hexahedral grids

Consider the unsteady compressible 2D Navier Stokes equations in conservative form

$$\frac{\partial Q}{\partial t} + \frac{\partial F}{\partial x} + \frac{\partial G}{\partial y} = 0 \tag{1}$$

where $Q$ is the vector of conserved variables; $F$ and $G$ are the total fluxes including both inviscid and viscous flux vectors.

To achieve an efficient implementation, all elements in the physical domain $(x, y)$ are transformed into a standard square element. $0 < \xi < 1$, $0 < \eta < 1$. The transformation can be written as:

$$\begin{pmatrix} x \\ y \end{pmatrix} = \sum_{i=1}^{K} M_i(\xi, \eta) \begin{pmatrix} x_i \\ y_i \end{pmatrix} \tag{2}$$

where $K$ is the number of points used to define the physical element, $(x_i, y_i)$ are the cartesian coordinates at those points, and $M_i(\xi, \eta)$ are the shape functions. The metrics and the Jacobian of the transformation can be computed for the standard element. The governing equations in the physical domain are then transfered into the computational domain, and the transformed equations take the following form:

$$\frac{\partial \tilde{Q}}{\partial t} + \frac{\partial \tilde{F}}{\partial \xi} + \frac{\partial \tilde{G}}{\partial \eta} = 0 \tag{3}$$

where $\tilde{Q} = |J| \cdot Q$ and

$$\begin{pmatrix} \tilde{F} \\ \tilde{G} \end{pmatrix} = |J| \begin{pmatrix} \xi_x & \xi_y \\ \eta_x & \eta_y \end{pmatrix} \begin{pmatrix} F \\ G \end{pmatrix} \tag{4}$$

In the standard element, two sets of points are defined, namely the solution points and the flux points, illustrated in figure 1. In order to construct a degree $(N-1)$ polynomial in each coordinate direction, solution at $N$ points are required. The solution points in 1D are chosen to be the Gauss points defined by:

$$X_s = \frac{1}{2}\left[1 - cos\left(\frac{2s-1}{2N} \cdot \pi\right)\right], s = 1, 2, \cdots, N. \tag{5}$$

The flux points were selected to be Legendre-Gauss quadrature points plus the two end points 0 and 1, as suggested by Huynh.[8] Choosing $P_{-1}(\xi) = 0$ and $P_0(\xi) = 1$, we can determine the higher-degree Legendre polynomials as

$$P_n(\xi) = \frac{2n-1}{n}(2\xi - 1)P_{n-1}(\xi) - \frac{n-1}{n}P_{n-2}(\xi) \tag{6}$$

The locations of these Legendre-Gauss quadrature points are the roots of equation $P_n(\xi) = 0$. They are generally found to be more stable than the Gauss-Lobatto flux points and produce more accurate solutions for high-order spectral difference schemes.

Using the solutions at $N$ solution points, a degree $(N-1)$ polynomial can be built using the following Lagrange basis defined as:

$$h_i(X) = \prod_{s=1, s\neq i}^{N} \left( \frac{X - X_s}{X_i - X_s} \right) \tag{7}$$

Similiarly, using the fluxes at $(N+1)$ flux points, a degree $N$ polynomial can be built for the flux using a similar Lagrange basis defined as:

$$l_{i+1/2}(X) = \prod_{s=0, s\neq i}^{N} \left( \frac{X - X_{s+1/2}}{X_{i+1/2} - X_{s+1/2}} \right) \tag{8}$$

The reconstructed solution for the conserved variables in the standard element is just the tensor products of the two one-dimensional polynomials,

$$Q(\xi, \eta) = \sum_{j=1}^{N} \sum_{i=1}^{N} \frac{\tilde{Q}_{i,j}}{|J_{i,j}|} h_i(\xi) \cdot h_j(\eta) \tag{9}$$

Similiarly, the reconstructed flux polynomials take the following form:

$$\begin{aligned} \tilde{F}(\xi, \eta) &= \sum_{j=1}^{N} \sum_{i=0}^{N} \tilde{F}_{i+1/2,j} \cdot l_{i+1/2}(\xi) \cdot h_j(\eta), \\ \tilde{G}(\xi, \eta) &= \sum_{j=0}^{N} \sum_{i=1}^{N} \tilde{G}_{i,j+1/2} \cdot h_i(\xi) \cdot l_{j+1/2}(\eta) \end{aligned} \tag{10}$$

The reconstructed fluxes are only element-wise continuous, but discontinuous across cell interfaces. For the inviscid flux, a Riemann solver is employed to compute a common flux at interfaces to ensure conservation amd stability. In our case, we have used the Rusanov solver[18] to compute the interface fluxes.

In summary, the algorithm to compute the inviscid flux derivatives consists of the following steps:

1. Given the conservative variables at the solution points, the conservative variables are computed at the flux points
2. The inviscid fluxes at the interior flux points are computed using the solutions computed at Step 1
3. The inviscid fluxes at the element interfaces are computed using the Rusanov solver.
4. The derivative of the fluxes are computed at the solution points according to (equation)

$$\left( \frac{\partial \tilde{F}}{\partial \xi} \right)_{i,j} = \sum_{r=0}^{N} \tilde{F}_{r+1/2,j} \cdot l'_{r+1/2}(\xi_i), \tag{11}$$

$$\left( \frac{\partial \tilde{G}}{\partial \eta} \right)_{i,j} = \sum_{r=0}^{N} \tilde{G}_{i,r+1/2} \cdot l'_{r+1/2}(\eta_j) \tag{12}$$

The viscous flux is a function of both the conserved variables and their gradients. Therefore, the solution gradients have to be calculated at the flux points. In our solver, the average approach described in reference[24] is used to compute the viscous fluxes. The procedure to compute the viscous fluxes can be described as follows.

1. Reconstruct $Q_f$ at the flux points from the $Q$ at the solution points using equation 9.
2. At the element interfaces, find the average of left and right values of $Q_f$; $\overline{Q_f} = \frac{1}{2}(Q_f^L + Q_f^R)$. For interior flux points, $\overline{Q_f} = Q_f$. Appropriate boundary conditions are applied at flux points on boundary edges.
3. Evaluate $\nabla Q$ at the solution points from $\overline{Q_f}$ using equation 11, where $\nabla Q = \left\{ \begin{array}{c} Q_x \\ Q_y \end{array} \right\}$ and $Q_x = \frac{\partial Q}{\partial \xi}\xi_x + \frac{\partial Q}{\partial \eta}\eta_x$, etc.
4. Reconstruct $\nabla Q$ to the flux points, apply appropriate boundary conditions for boundary flux points, and average them on the element interfaces as $\overline{\nabla Q_f} = \frac{1}{2}(\nabla Q_f^L + \nabla Q_f^R)$
5. Use $\overline{Q_f}$ and $\overline{\nabla Q_f}$ in order to compute viscous flux vectors at the flux points.

It should be mentioned that all explicit time-marching calculations for steady flows have been done using a Jameson type four-stage Runge Kutta scheme (RK4), which is 2nd order accurate in time. For the unsteady problems, we have used a 4th order accurate, strong-stability-preserving five-stage Runge-Kutta scheme[21] to advance in time.

## III. Artificial Viscosity

The application of spatially high-order schemes to compute flows with discontinuities such as shock or contact-discontinuities, results in non-physical spurious oscillations that make the computation unstable. One of the major concerns in simulating such flows is to ensure the removal of these non-physical oscillations while avoiding damping of the resolved scales of turbulence.

The present study uses an artificial viscosity approach similar to the 'Local artificial viscosity and diffusivity' approach of Kawai and Lele.[9] This method is a modification of the original high-wavenumber biased artificial viscosity approach introduced by Cook and Cabot,[6] extended to anisotropic and curvilinear structured grids.

The present artificial viscosity approach adds grid-dependent components to the viscosity coefficients, as proposed by Kawai and Lele,

$$\begin{aligned} \mu &= \mu_f + \mu_\Delta, \\ \beta &= \beta_f + \beta_\Delta, \\ \kappa &= \kappa_f + \kappa_\Delta \end{aligned} \tag{13}$$

where $\mu$ is the dynamic (shear) viscosity, $\beta$ is the bulk viscosity, and $\kappa$ is the thermal conductivity. The $f$ and $\Delta$ subscripts denote the fluid and artificial transport coefficients respectively.

These artificial transport coefficients are defined by:

$$\begin{aligned} \mu_\Delta &= C_\mu \rho \, \overline{| \sum_{l=1}^{3} \sum_{m=1}^{3} \Delta_l^{r+2} \left( \frac{\partial \xi_l}{\partial x_m} \right)^r \frac{\partial^r S}{\partial \xi_l^r} |} \\ \beta_\Delta &= C_\beta \rho \, \overline{| \sum_{l=1}^{3} \sum_{m=1}^{3} \Delta_l^{r+2} \left( \frac{\partial \xi_l}{\partial x_m} \right)^r \frac{\partial^r (\nabla . \mathbf{u})}{\partial \xi_l^r} |} \\ \kappa_\Delta &= C_\kappa \frac{\rho c_s}{T} \, \overline{| \sum_{l=1}^{3} \sum_{m=1}^{3} \Delta_l^{r+2} \left( \frac{\partial \xi_l}{\partial x_m} \right)^r \frac{\partial^r e}{\partial \xi_l^r} |} \end{aligned} \tag{14}$$

where $C_\mu$, $C_\beta$ and $C_\kappa$ are user-specified constants. $\xi_l$ refers to the computational coordinates and $x_m$ refer to the physical coordinates. $\Delta_l$ is the physical grid spacing along a grid line in the $\xi_l$ direction. The magnitude of the strain rate tensor ($S$), the dilatation ($\nabla.\mathbf{u}$) , and the internal energy ($e$) are the sensors corresponding to artificial shear viscosity, bulk viscosity and conductivity respectively. It is suggested that r equals 4 or higher. For sufficiently high $r$, the high-wavenumber bias ($k^r$) results in damping of wavenumbers close to the unresolved wavenumbers. The overbar denotes a filter to smooth the artificial transport coefficients. In

structured grid calculations, a truncated Gaussian filter is used.[6] The filter is also meant to eliminate cusps introduced by the absolute value operator, which in turn ensures that artificial viscosities are positive.

An advantage of such an artificial viscosity scheme is that it eliminates the need for limiters and switches to turn off the artificial bulk viscosity in regions of expansion and isentropic compression. Also, the artificial shear viscosity is automatically zero in regions of uniform shear. The artificial viscosity/conductivity is calculated at each flux point. This is computationally extensive, but it ensures smooth variation of artificial transport coefficients. A smooth representation of artificial viscosity within mesh elements is considered beneficial as compared to the piecewise-constant artificial viscosity formulations, as element-to-element variations can lead to oscillations in state gradients and disparate equilibrium shock-jump conditions in neighboring elements.

The steps involved in the implementation of the artificial viscosity method to the SD solver can be explained as follows. Consider the calculation of artificial shear viscosity.

1. The sensor $S$ (strain rate) is computed at the solution points.
2. It is then extrapolated to the flux points.
3. $\frac{\partial S}{\partial \xi_l}$ is computed at the solution points, and then reconstructed to the flux points.
4. Another differentiation operation, gives $\frac{\partial^2 S}{\partial \xi_l^2}$ at the solution points.
5. The above steps can be repeated required number of times to obtain $\frac{\partial^r S}{\partial \xi_l^r}$ at the solution points.
6. Similarly, the partial derivatives of the other sensors can also be computed.
7. The artificial transport coefficients are computed at the solution points using equations (14).
8. The coefficients are then filtered and reconstructed to the flux points.

### III.A. Filter for unstructured SD setup

The filter plays an important role in artificial viscosity computations as it ensures smooth variation of artificial transport coefficients within the domain. For calculations using artificial viscosity on structured grids, a truncated Gaussian filter is used. A 7-point or 9-point stencil is generally used for this purpose.[6] For calculations in 2D, the Gaussian filter is applied along each grid-line separately. However, for unstructured grids it is not reasonable to implement the Gaussian filter in its existing form, as obtaining a stencil for each solution/flux point can be tedious. The stencil would lie across cells, and the non-uniform spacing would have to be taken into account, thus making it cumbersome to implement. This motivated the development of a filter that would be suited to the current SD setup.

In the current study we use an element-wise restriction-prolongation filter (we will refer to it as the R-P filter). The concept is similar to the one used by Blackburn et al[4] for spectral element filtering. It involves the projection of the quantity in concern to a lower-order basis (restriction), smoothing at this level, and then extrapolation back to original basis (prolongation). The basic steps in implementation of the R-P filter can be described in 1-D as follows,

1. Consider a 4th order SD element. The artificial viscosity terms have been computed at the 4 solution points (Figure 2(a)).
2. The function (represented by a cubic polynomial through the 4 solution points) is restricted to 2 solution points (corresponding to 2nd order SD) (Figure 2(a)). The polynomial fit through the interpolated function is reduced to linear. The function is now extrapolated to the 3 flux points corresponding to second order solution.
3. The function values are averaged at the interface for all element interfaces (Figure 2(c)). This is equivalent to smoothing of the function at the lowest level. A quadratic polynomial is fitted through this smoothed function through the 3 flux points.
4. It is then extrapolated to the flux points at the highest level (4th order)(Figure 2(d)).

It was found that in 1-D, this filter performs comparably to the Gaussian filter applied on flux points. Since the solution representation in multiple dimensions is just a tensor product of 1-D polynomials, the extension of this filter to 2-D and 3-D is straight-forward.

Figure 3 corresponds to the initial condition of the SOD shock tube case with a density discontinuity at x=0.5. The artificial conductivity is non-zero in the vicinity of x=0.5. The figure shows that prior to filtering the artificial conductivity field is noisy and may have oscillatory behavior. The filtered coefficient is smoother and results in a better solution. Also, smoothing effect of the present R-P filter compares quite well with the Gaussian filter, even though the peaks do not match.

# IV. Results

It must be mentioned that the Spectral Difference scheme has been implemented in 1D, 2D and 3D solvers which have been tested, validated and found to exhibit formal order accuracy.[10,16] In this section, the results obtained from the application of Spectral Difference with artificial viscosity to problems with shocks, are discussed. Firstly, two 1-D cases are demonstrated, namely the SOD shock-tube case, and the Shu-Osher shock-entropy wave interaction case. Then the application of artificial viscosity for shock-capturing in 2D is demonstrated with the reflecting oblique shock wave test-case and the supersonic flow past bump test-case.

## IV.A. SOD Shock-tube problem

The first 1-D test case is the shock-tube problem introduced by SOD.[20] The initial left and right-side conditions are $\rho_l = 1.0$, $u_l = 0.0$ and $p_l = 1.0$ for $x \leq 0.5$, and $\rho_r = 0.125$, $u_r = 0.0$ and $p_r = 0.1$ for $x > 0.5$. Simulations are performed on a uniformly spaced grid in the region $0 \leq x \leq 1$. Artificial bulk viscosity and conductivity are used. The coefficients used were $C_\beta = 0.06$ and $C_\kappa = 0.01$, along with r=2 (in equation 14), corresponding to second order derivatives of the sensor quantities. $C_\mu$ was set to zero.

Figure 4 (a),(b) and 5 (a) shows the comparison between density, velocity and pressure for the exact solution and 4th order SD computation with 100 cells at time $\tau = 0.15$. The shock and the contact discontinuity are captured well without significant spurious oscillations, and show reasonable agreement with the exact solution. Figure 5 (b) shows the variation of density profile with grid-refinement. It is observed that as the grid is refined, the solution converges closer to the exact solution. It should also be noted that for all grid spacings, the shock is spread over two cells and the contact discontinuity is spread over 3 cells. Figure 6 (a) shows the artificial bulk viscosity coefficient. It is seen to be maximum in the vicinity of the shock. Figure 6 (b) shows the artificial conductivity. There are two peaks corresponding to the shock and the contact discontinuity. In the SOD problem, artificial conductivity plays an important role because the artificial viscosity sensor does not sense the contact discontinuity.

The results described above were obtained using $r = 2$ in the artificial transport coefficient calculations. Computations were also conducted using $r = 4$, but the results obtained were very similar to those obtained for $r = 2$. For $r = 4$, $C_\beta = 0.001$ and $C_\kappa = 0.0001$ were used. For both 1-D cases it was observed that $r = 2$ and $r = 4$ gave very similar results. In fact, it is necessary to use $r = 4$ or higher only when there is shock-turbulence interaction. For all cases considered in this study, $r = 2$ has been used.

## IV.B. Shu-Osher problem

The second 1-D test case is the shock-entropy wave interaction introduced by Shu and Osher.[19] Because the entropy waves are sensitive to the numerical dissipation, excessive numerical dissipation damps the entropy waves. Initial left and right side conditions are given by: $\rho_l = 3.857143$, $u_l = 2.629369$ and $p_l = 10.33333$ for $x < -4$, and $\rho_r = 1 + 0.2 * sin(5x)$, $u_r = 0.0$ and $p_r = 1.0$ for $x \geq -4$. Simulations are performed on a uniformly spaced grid in the region $-5 \leq x \leq 5$. The coefficients used are the same as for the SOD case.

Figure 7(a) shows the comparison between the reference solution and 4th order SD simulations with 100, 200 and 400 cells. The reference solution is obtained using 5th order WENO on 2000 grid points. The density profile using 400 cells shows excellent agreement with the reference solution. Figure 7(b) shows a close up of the density plot in the region of the entropy waves. It is found that solution with 200 cells also shows reasonable agreement with reference solution. Figures 8(a) and (b) show the velocity and pressure profiles behind the shock.

### IV.C. Two-dimensional oblique shock-reflection

The first 2-D shock test case is the oblique shock reflection on an inviscid wall. The free-stream Mach number is 3 and the oblique shock angle is 33°. The computational domain extends from $x = -1.5$ to $x = 1.5$ and $y = 0$ to $y = 1$. Supersonic inlet and outlet boundary conditions are used. The exact shock jump conditions corresponding to oblique shock at $M = 3, \alpha = 33°$ at $x = -1$, are imposed on the upper boundary. The lower boundary is an inviscid wall.

Third order SD simulations were conducted. Figure 9 shows the pressure contours obtained using a $60 \times 20$ mesh (1200 cells). The next figure ( Figure 10 ) gives a comparison of pressure contours obtained using the coarse mesh and a finer $120 \times 40$ mesh (4800 cells). As expected the finer mesh gives a sharper shock profile, and smoother pressure contours. Pressure profiles along the $y = 0.18$ line for both meshes are shown in figure 11. They pressure profiles compare well with the pressure profile obtained using artificial viscosity with 6th order Compact Difference on a structured $301 \times 101$ mesh.[9]

The above computations were computed using r=2 and $C_\beta = 0.01$. Also, the artificial shear viscosity and artificial conductivity are set to zero. This is because there are no large shear gradients, and no contact discontinuities, and hence artificial bulk viscosity is sufficient to stabilize the calculations.

### IV.D. Inviscid Supersonic flow past bump

This test-case consists of inviscid supersonic flow in a channel with a 4% thick circular bump on the bottom. The length of the channel is 3 units and its height 1 unit. The inlet Mach number is 1.4. This test case has been used by Ripley et al.[17] in computations using adaptive unstructured mesh refinement. Third and fourth order SD computations were conducted on two meshes. The coarse computational mesh has 1200 elements, and 20 nodes to resolve the bump, as depicted in figure 12. The fine mesh has 4800 cells, and has twice the number of nodes in the x and y directions. The surface of the bump is represented as a quadratic and cubic boundary for third and fourth order calculations respectively.

The pressure contours obtained using the 3rd order SD scheme with artificial viscosity on the coarse mesh is shown in figure 13, and compares well with those obtained using adaptive unstructured mesh refinement.[17] The pressure contours obtained for the fine mesh are shown in figure 14. It is observed that on the finer mesh, the shock profiles are sharper, and smoother contours are obtained. Figure 15 shows the drop in global residual, indicating a stable, convergent solution for both 3rd and 4th order cases. It must be mentioned that in the absence of artificial viscosity, the solution develops spurious oscillations and the simulation becomes unstable.

Figure 16 shows the pressure along the horizontal line corresponding to $y = 0.4$ units. It is observed that the shocks are resolved sharply, without any significant spurious oscillations. Also note that the first two shocks are captured within two cells for both the coarse and fine mesh. The last pressure jump lies close to the joining point of two oblique shocks and hence is not resolved on the coarse mesh. However, on the finer mesh, two distinct shock pressure jumps are obtained. Figure 17 gives a plot of the sensor, which is the dilatation in this case. The dilatation is highly negative in the region of shocks. Figure 18 shows the variation of artificial bulk viscosity. We see that artificial viscosity is added only in regions with sharp gradients of dilatation, corresponding to shocks.

Figure 19 shows the pressure contours obtained using 4th order SD. It is observed that the shock profiles are slightly sharper than in the case of the third order computation. Also, 4th order on finer mesh gives sharper shock resolution and more accurate contours in comparison to the coarse mesh (see Figure 20).

## V. Conclusions and Future work

A high wave-number biased artificial viscosity scheme has been implemented in order to enable high-order computation of flows with discontinuities. The application of artificial viscosity with the Spectral Difference method for the computation of flows with shocks is demonstrated with test cases in 1D and 2D. Promising results have been obtained for these cases, with the method being able to produce a stable solution with sharp resolution of shocks, and no significant spurious oscillations. An element-based restriction-prolongation filter has been developed. Further efforts will be directed towards the testing and validation of the proposed method, using a variety of shock-related problems in 2D. Efforts will also be directed towards the study of the effect of using irregular meshes, and the effect of adding artificial viscosity on the global accuracy of

the Spectral Difference scheme. The scheme will then be used to tackle problems with shocks and shock-turbulence interaction in three dimensions.

## VI. Acknowledgements

The authors would like to thank the grant support from NSF monitored by Dr Leland Jameson (with award number 0708071), and AFOSR monitored by Dr Fariba Fahroo (with award number FA9550-07-1-0195).

## References

[1]F. Bassi & S. Rebay, A high-order accurate discontinuous finite element method for the numerical solution of the compressible Navier-Stokes equations, *Journal of Computational Physics*, Vol. 131, pp.267-279, 1997

[2]F.Bassi and S. Rebay, High-order accurate discontinuous finite element solution of the 2D euler equations, *Journal of Computational Physics*, Vol. 138, pp. 251-285, 1997

[3]G.E. Barter & D.L. Darmofal, Shock Capturing with Higher-Order, PDE-Based Artificial Viscosity, *AIAA paper*, AIAA-2007-3823, 2007.

[4]H.M.Blackburn & S. Schmidt, Spectral Element filtering tecniques for large eddy simulation with dynamic estimation, *Journal of Computational Physics*, Vol. 186, pp.610-629, 2003

[5]A. W. Cook & W. H. Cabot, A high-wavenumber viscosity for high-resolution numerical methods *Journal of Computational Physics*, Vol. 195, pp.594-601, 2004.

[6]A. W. Cook & W. H. Cabot, Hyperviscosity for shock-turbulence interactions *Journal of Computational Physics*, Vol. 203, pp.379-385, 2005.

[7]B. Fiorina & S.K. Lele, An artificial nonlinear diffusivity method for supersonic reacting flows with shocks, *Journal of Computational Physics*, Vol. 222, pp. 246-264, 2007.

[8]H.T. Huynh, A Flux Reconstruction Approach to High-Order Schemes Including Discontinuous Galerkin Methods, *AIAA paper*, AIAA-2007-4079, 2007.

[9]S. Kawai & S.K. Lele, Localized Artificial Diffusivity Scheme for Discontinuity Capturing on Curvilinear Meshes,*Journal of Computational Physics*, Vol. 227, pp.9498-9526, 2008.

[10]C. Liang, S. Premasuthan, A. Jameson & Z. Wang, Large Eddy Simulation of Compressible Turbulent Channel Flow with Spectral Difference method, *AIAA paper*, 2009-402, 2009

[11]Y. Liu, M. Vinokur, & Z. J. Wang, Spectral difference method for unstructured grids I: Basic formulation, *J. of Comput. Phys.*, Vol. 216, pp. 780-801, 2006.

[12]Y. Liu, M. Vinokur, & Z. J. Wang, Spectral (finite) volume method for conservation laws on unstructured grids V: Extension to three-dimensional systems, *Journal of Computational Physics*, Vol. 212, pp 454-472, 2006.

[13]H. Luo, J. D. Baum and R. Löhner, A p-multigrid discontinuous Galerkin method for the Euler equations on unstructured grids, *Journal of Computational Physics*, Vol. 211, pp 767-783, 2006.

[14]J. von Neumann, & R. Richtmyer, A method for the numerical calculation of hydrodynamic shocks, *Journal of Applied Physics*, Vol. 21, pp.232237, 1950.

[15]P.-O. Persson & J. Peraire, Sub-Cell Shock Capturing for Discontinuous Galerkin Methods, *AIAA paper*, AIAA-2006-112, 2006.

[16]S. Premasuthan, C. Liang, A. Jameson & Z. Wang, p-Multigrid Spectral Difference Method For Viscous Compressible Flow Using 2D Quadrilateral Meshes, *AIAA paper*, 2009-950, 2009

[17]R.C. Ripley, F.S. Lien & M.M. Yoyanivich, Adaptive Unstructured Mesh Refinement of Supersonic Channel Flows, *International Journal of Computational Fluid Dynamics*, Vol. 18 (2), pp.189198, 2004

[18]V.V. Rusanov, Calculation of interaction of non-steady shock waves with obstacles, *Journal of Computational and Mathematical Physics USSR*, Vol. 1, pp. 267279, 1961.

[19]C.W.Shu & S.J.Osher, Efficient implementation of essentially nonoscillatory shock capturing schemes II, *Journal of Computational Physics*, Vol. 83, pp.32-78, 1981

[20]G.A.Sod, A survey of several finite difference methods for sytems on non-linear hyperbolic conservation laws, *Journal of Computational Physics*, Vol. 27, pp.1-31, 1981

[21]R. J. Spiteri, S. J. Ruuth, A new class of optimal high-order strong-stability-preserving time discretization methods, *SIAM J. Numer. Anal.*, Vol 40, pp 469-491, 2002

[22]Y. Sun, Z. J. Wang, & Y. Liu, Efficient Implicit LU-SGS Algorithm for high-order spectral difference method on unstructured hexahedral grids, *AIAA paper*, AIAA-2007-313, 2007.

[23]Z.J. Wang, Y. Liu, G. May and A. Jameson, Spectral Difference Method for Unstructured Grids II: Extension to the Euler Equations, *Journal of Scientific Computing*, Vol. 32, pp. 45-71, 2007.

[24]Y. Sun, Z. J. Wang, & Y. Liu, High-order multidomain spectral difference method for the Navier-Stokes equations on unstructured hexahedral grids, *Communication in Computational Physics*, Vol. 2, pp. 310-333, 2007.

[25]Z. J. Wang & Y. Liu, Extension of the spectral volume method to high-order boundary representation, *Journal of Computational Physics*, Vol. 211, pp. 154-178, 2006.

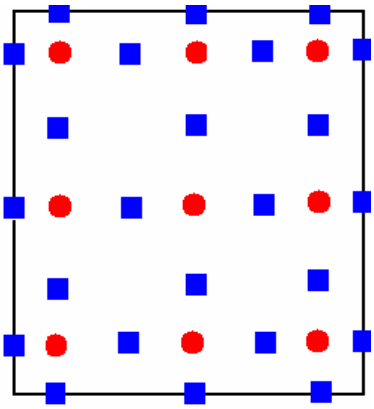

**Figure 1. Position of solution (circles) and flux (squares) points on standard square element for 3rd order SD**

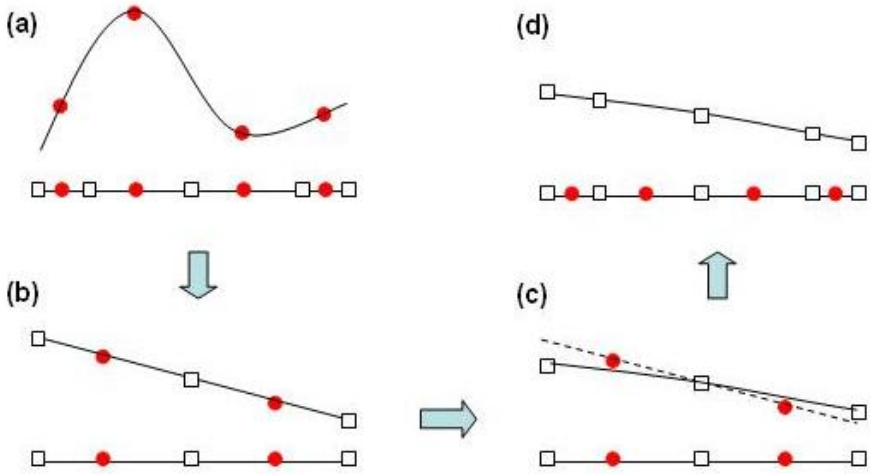


**Figure 2. Steps involved in implementation of filter for 4th order SD**

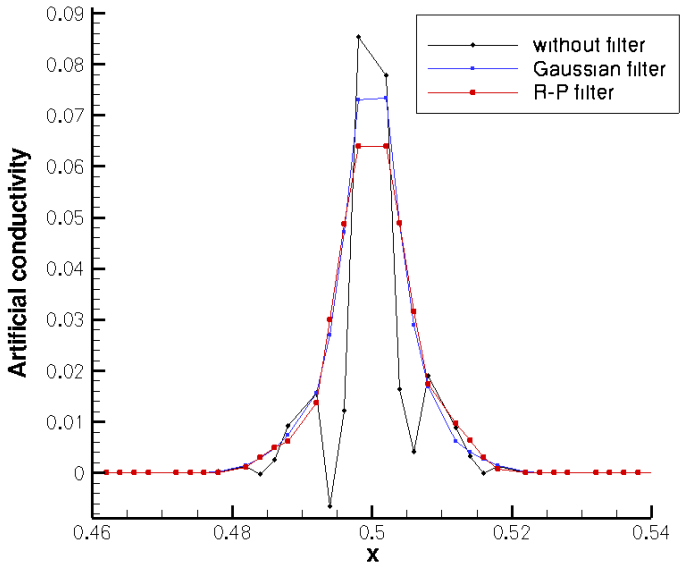


**Figure 3. Effect of filtering on the smoothness of artificial viscosity/conductivity coefficients**

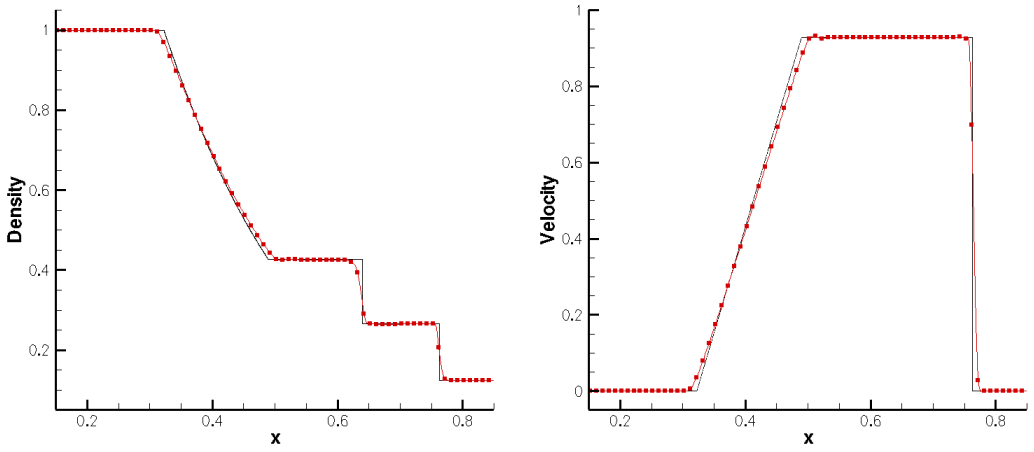


(a) (b)

**Figure 4. SOD shock tube case, black line - exact solution, red line - 4th order SD with 100 cells at $\tau = 0.15$ (a) density vs. x ; (b) velocity vs. x.**

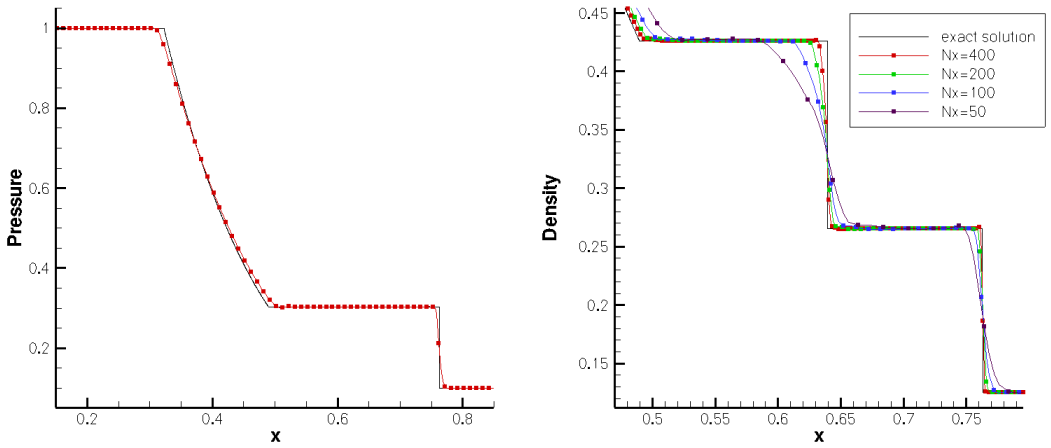


(a) (b)

**Figure 5. SOD shock tube case, (c) pressure vs. x ; (d) effect of grid-refinement on density (Nx=number of cells).**

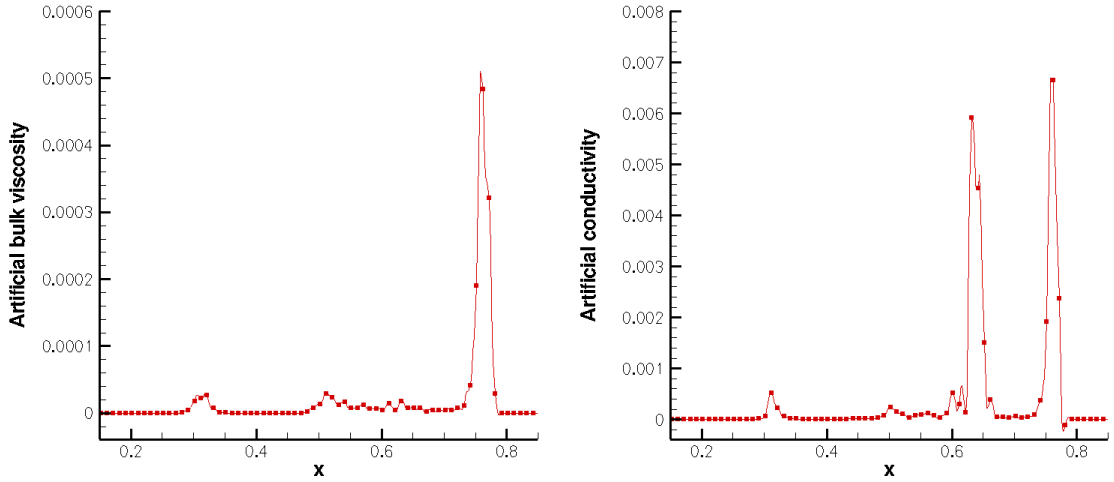


(a) (b)

**Figure 6. SOD shock tube case (a) Artificial bulk viscosity; (b) Artificial conductivity at $\tau = 0.15$**

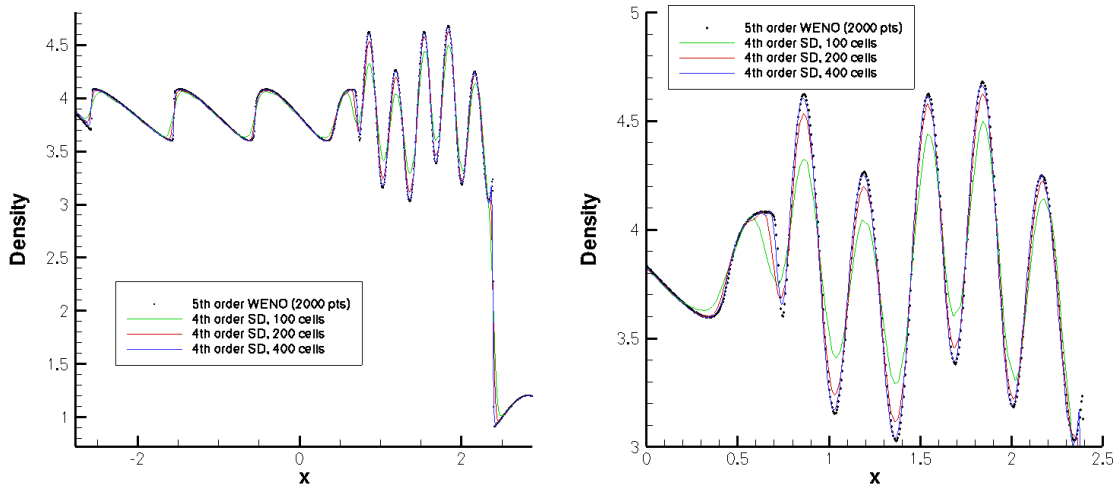


**Figure 7. Shu-Osher Shock turbulence interaction. Density is presented at $\tau = 1.8$.**

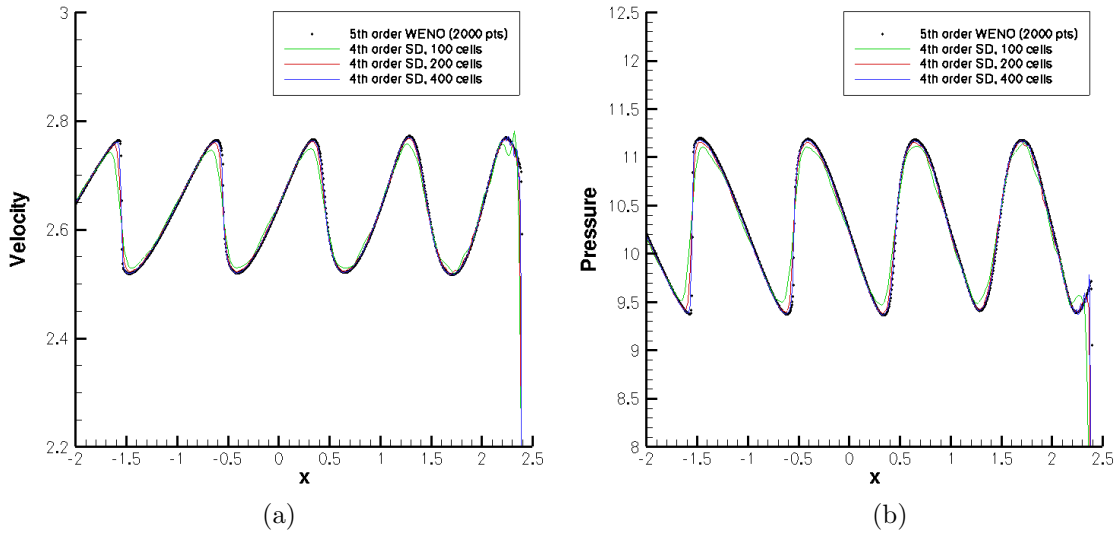


**Figure 8. Shu-Osher Shock turbulence interaction. Plot of (a)Velocity, (b)Pressure, at $\tau = 1.8$.**

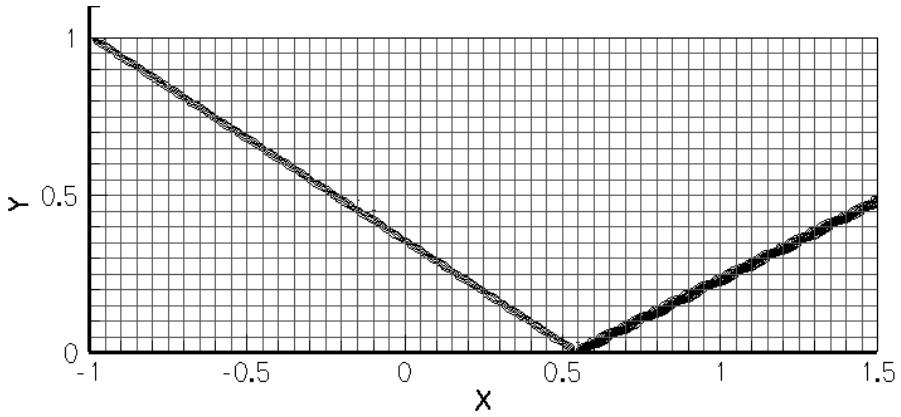


**Figure 9. Computational mesh and pressure contours for reflecting oblique shock test case. 20 equally spaced contours between 1 and 7.2**

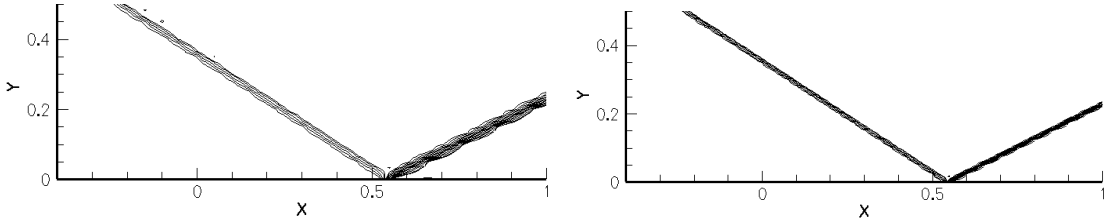


**Figure 10. Comparison of pressure contours for (a)$60 \times 20$ mesh, (b)$120 \times 40$ mesh.**

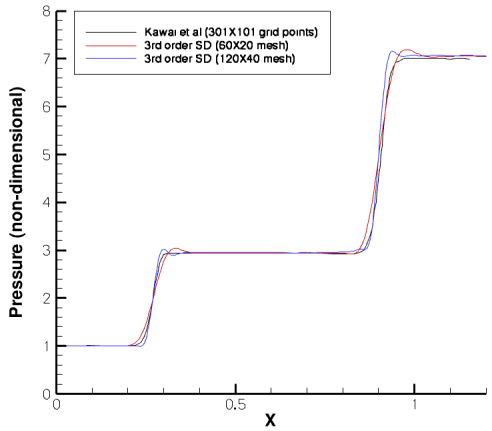


**Figure 11. Non-dimensional pressure along y=0.18. Comparison with 6th order Compact Difference with artificial viscosity[9]**

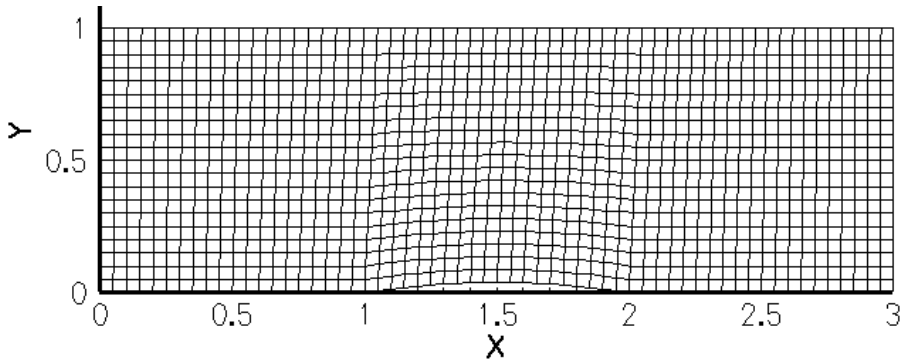


**Figure 12. Computational grid for supersonic flow past bump (thickness=4%)**

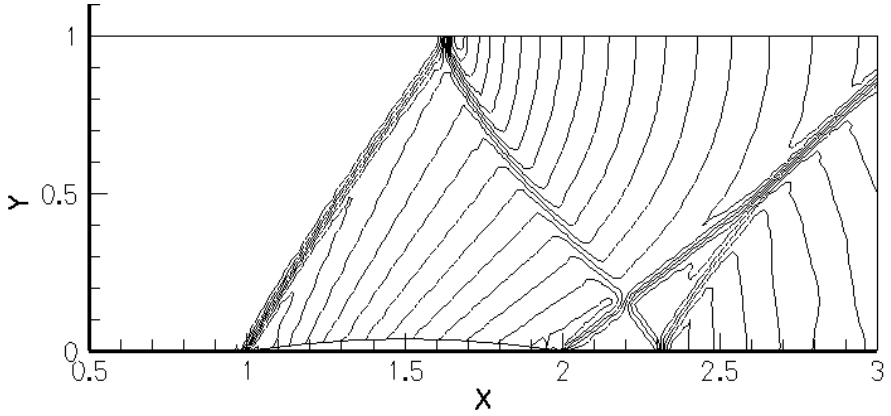


**Figure 13. Non-dimensional pressure contours obtained using artificial viscosity with 3rd order SD on the $60 \times 20$ mesh. 20 equally spaced contours from 0.6 to 2.00**

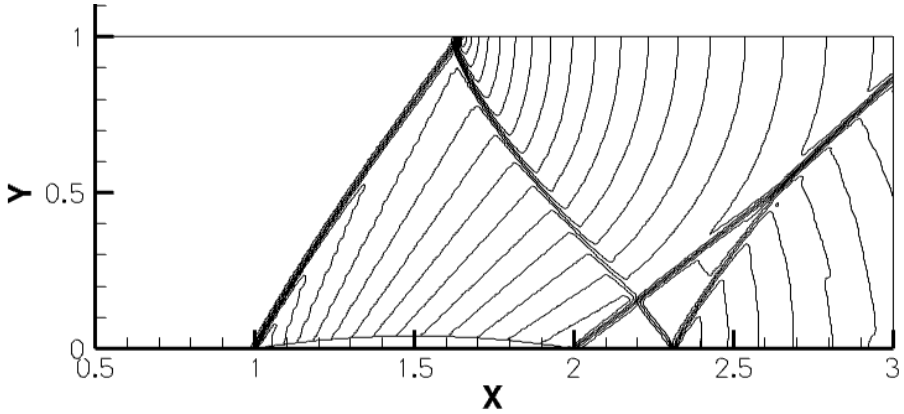


**Figure 14. Non-dimensional pressure contours obtained using artificial viscosity with 3rd order SD on the $120 \times 40$ mesh. 20 equally spaced contours from 0.6 to 2.00**

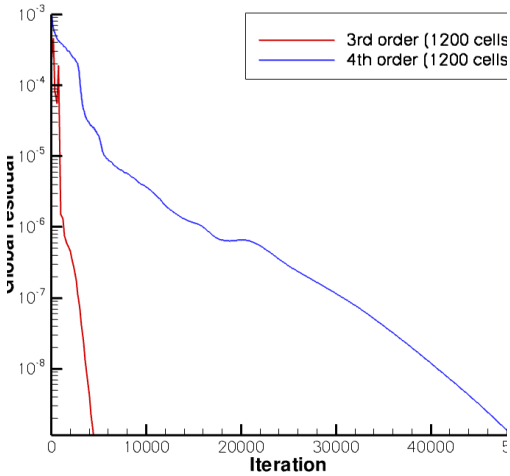


**Figure 15. Convergence plot for supersonic bump flow case 3rd and 4th order SD with artificial viscosity**

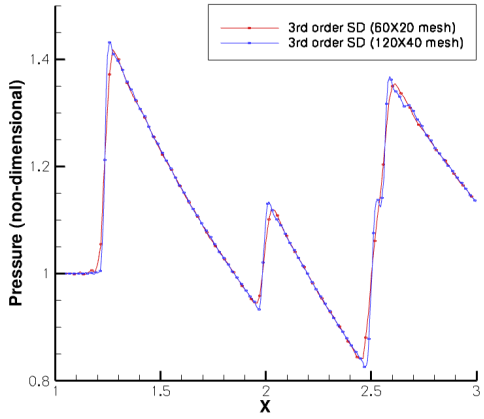


**Figure 16. Non-dimensional pressure along y=0.4 line using 3rd order SD**

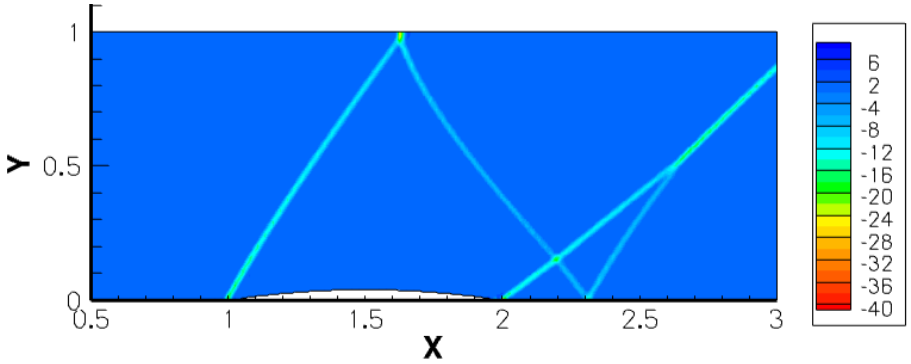


**Figure 17. Plot of the dilatation sensor for 3rd order SD computation on $120 \times 40$ mesh**

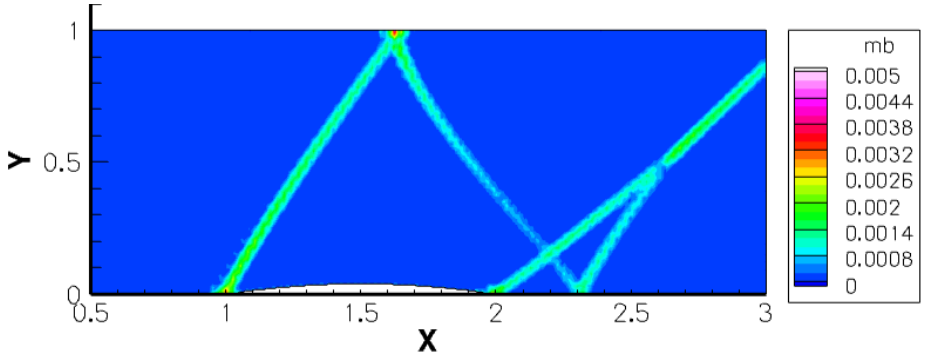


**Figure 18. Plot of the artificial bulk viscosity for 3rd order SD computation on $120 \times 40$ mesh**

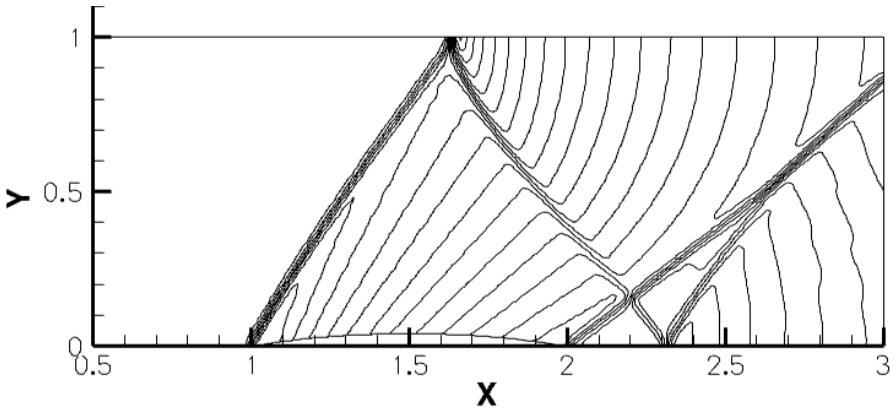


**Figure 19. Non-dimensional pressure contours obtained using artificial viscosity with 4th order SD on the $60 \times 20$ mesh. 20 equally spaced contours from 0.6 to 2.00**

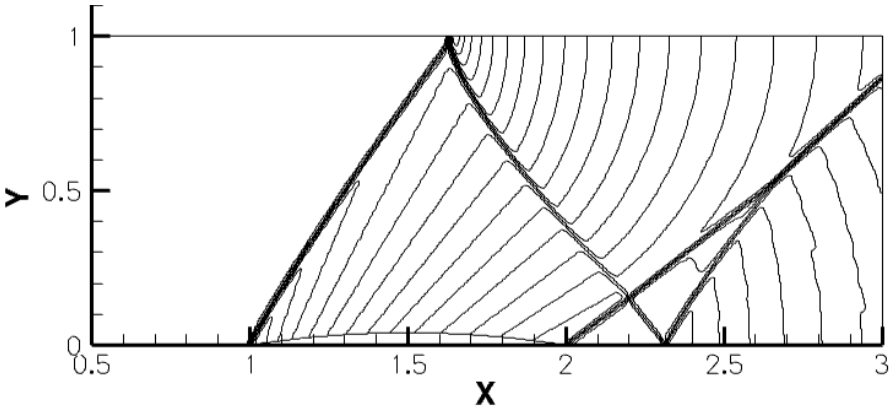


**Figure 20. Non-dimensional pressure contours obtained using artificial viscosity with 4th order SD on the $120 \times 40$ mesh. 20 equally spaced contours from 0.6 to 2.00**